PERGAMON

International Journal of Heat and Mass Transfer 44 (2001) 2845–2862

International Journal of HEAT and MASS TRANSFER

www.elsevier.com/locate/ijhmt

Thermal analysis of the laser surface transformation hardening process

R. Komanduri *, Z.B. Hou

School of Mechanical & Aerospace Engineering, Oklahoma State University, Stillwater, OK 74078-5016, USA

Received 16 March 2000; received in revised form 11 October 2000

Abstract

An analytical solution for the temperature rise distribution in laser surface transformation hardening of a steel workpiece of finite width is developed based on Jaeger's classical moving heat source method [Proc. Roy. Soc. NSW 76 (1942) 203] and Carlsaw and Jaeger [Conduction of heat in solids, Oxford University Press, Oxford, UK, 1959] to predict the optimal operational parameters. The laser beam is considered as a moving plane (disc) heat source with a pseudo-Gaussian distribution of heat intensity. It is a general solution in that it is applicable for both transient and quasi-steady state conditions. The effect from two boundaries of the workpiece of finite width is included in the analysis. The solution can be used to determine the temperature rise distribution in and around the laser beam heat source on the work surface as well as with respect to depth at all points including those very close to the heat source. The width and depth of the melt pool (MP) and the hardening zone near the surface of the workpiece with finite width can also be calculated under transient and quasi-stationary conditions. The analytical model developed here can be used to determine the time required for reaching the quasi-steady state. Steen and Courtney [Metals Technol. (December 1979) 456] reported a five level, full factorial experiments of laser surface transformation hardening. They considered the surface temperatures and the depth of hardening as approximate functions of the laser input parameters, namely, the laser beam power, P, the laser beam diameter, D_e, and the traverse velocity of the beam, v. A comparative study is made on the analytical approach presented here with the multi-parameter experimental and the semi-empirical approach by Steen and Courtney. While good agreement was found between the results of the analytical work and the semi-empirical approach for the case of scanning velocity for no surface melting, significant differences were found for the laser transformation hardening for a depth of hardening of 0.1 mm. This was due to the nature of the semi-empirical relationships considered by Steen and Courtney for each case. For example, the traverse velocity was assumed to be proportional to P/D_b^2 (i.e., power intensity) for no surface melting which has some physical significance, while it was assumed to be proportional to P^2/D_b for laser transformation hardening for a depth of hardening of 0.1 mm, for which there is no physical or analytical basis. Steen and Courtney developed semi-empirical equations based on the regression analysis of the experimental data, while the analytical solutions presented here are exact. The analytical solutions provide a better appreciation of the physical relationships between the relevant laser parameters and the width of the workpiece. The analysis facilitates the prediction and optimization of the process parameters for practical applications.

Keywords: Laser surface hardening; Thermal analysis; Moving heat source; Heat treatment

1. Introduction

Lasers are increasingly finding broader industrial applications in materials processing, including cutting, drilling, welding, heat treatment, and surface alloying, to name a few [1]. This is partly due to a better understanding of the fundamentals of laser–material

* Corresponding author. Tel.: +1-405-744-5900; fax: +1-405-744-7873.

E-mail address: ranga@ceat.okstate.edu (R. Komanduri).

0017-9310/01/$ - see front matter
PII: S0017-9310(00)00316-1

Nomenclature

a	thermal diffusivity of the medium, cm^2/s
q_{rg}	heat liberation rate of a ring heat source, J/s
q_{pl}	heat liberation rate of a moving disc heat source, J/s
q_0	heat liberation intensity of a moving disc heat sources, J/cm^2 s
R_0	distance between the center of the moving disc heat source and the point where the temperature rise at time t is concerned, cm
R_1, R_2	distances between the center of the image moving disc heat sources and the point where the temperature rise at time t is concerned, cm
X_0	projection of the distance on the X-axis between the center of the moving disc heat source and the point where the temperature rise at time t is concerned, cm
X_1, X_2	projection of the distances on the X-axis between the center of relevant image moving disc heat sources and the point where the temperature rise at time t is concerned, cm
t	time of observation or the time after the initiation of a moving disc heat source, s
X, y, z	coordinates of any point M in a moving coordinate system where the temperature rise is concerned
P	laser beam power, W
D_b	laser beam diameter, cm
v	scanning velocity, cm/s
r_0	radius of the moving disc heat source or moving ring heat source, cm
r_i	radius of a segmental ring heat source, cm
λ	thermal conductivity of the medium, J/cm s °C
θ_M	temperature rise at any point M and at any time t, °C
ρ	density of the medium, g/cm^3
$I_0(p)$	modified Bessel function of first kind order zero $= \frac{1}{2\pi}\int_0^{2\pi} e^{p\cos\alpha}\,d\alpha$

interactions and partly due to the advances in the laser technology including the availability of lasers as a fully integrated, computer-controlled or numerically controlled (NC), automated, turn-key systems, in many cases. The latter relieves the user from taking expensive and difficult steps of integrating the laser with the rest of the system for a given application. Heat treatment or surface transformation hardening of steels, which is the subject of this investigation, is a particularly attractive application for industrial lasers in view of the vast usage of steel for a myriad of applications and the fact that a fine laser beam enables selective hardening (to a required depth and width). For example, in laser hardening of gears (Fig. 1), hardening is needed only at sites of excessive wear (using a laser beam of relatively small diameter) without affecting the desirable toughness of the underlying substrate material. All this can be accomplished in an automated system effectively and economically. As heating is from the surface, the effect is highly localized thereby reducing thermal distortions to a minimum. Other advantages of laser heat treatment include: high processing speeds, selective area treatment, accessibility to remote areas via appropriate laser optics, requirement of no external quenching media (the rapid heating and cooling rates with the laser enables transformation of the steel into austenite initially and self-quenching of steel (by conduction into the cold substrate material underneath) resulting in the transformation of it into martensite, no chemical contamination, versatility, and the ability of the laser to be fully automated using either a numerical control (NC) or a computer-controlled system [1]. Typically, a minimum interaction time of 10^{-2} s, a power density of $>10^3$ W/cm^2, and a

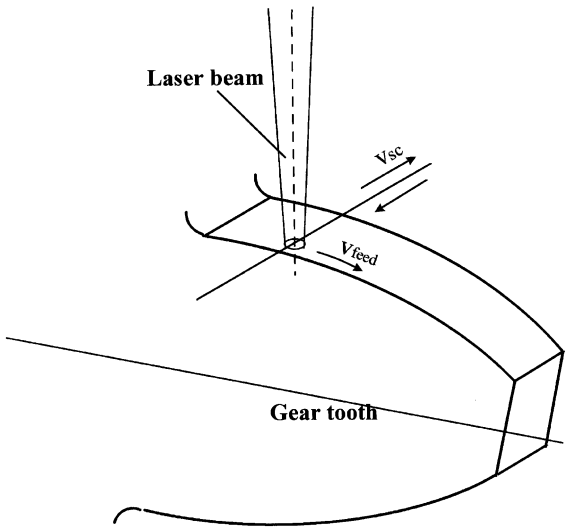

Fig. 1. Schematic of the laser surface transformation hardening of gears.

traverse speed of 5–50 mm/s are required for transformation hardening of steels [1]. No melting is involved or rather should be avoided in laser surface hardening which sets one limit on the magnitude of the process parameters. However, the temperatures should be high enough and the duration long enough for the transformation of steel into austenite. For example, if the work material is a medium to high carbon steel, the temperature of the surface layer during heat treatment should be >780°C (critical phase transition temperature of high carbon steel, Ac3). For various quenchable alloy

steels, it is in the range of ~800–900°C. Following this, the cooling rate should be fast enough (~10^3°C/s) for quenching to take place that will enable the transform of austenite into martensite. This sets the other limit on the magnitude of the process parameters. Thus, it is possible to set the operating regime of the process parameters for the laser surface transformation hardening process, as will be shown in this investigation.

The major processing parameters for laser surface heat treatment include laser beam power, laser beam diameter, distribution of power (or heat intensity distribution) across the beam, laser beam absorptivity into the work material, traverse speed of the laser beam across the substrate surface, and the thermal properties of the work material. To reduce reflectivity, some type of absorbent coating, such as a colloidal graphite coating, a mixture of potassium and sodium silicate coating, or a phosphate coating is almost always used. As a result, the surface absorptivity is ~80% in most cases [1,2]. In this investigation, a surface absorptivity of ~80% is assumed in the analysis on this basis. The dependent variables are the depth of hardening, geometry of the heat affected zone (HAZ) and the microstructure, and the properties and performance of the resulting heat treated material in service. For a better appreciation of the laser heat treatment process and a wider application of it in industry, it is necessary to establish appropriate relationships between the output variables and the input parameters. It is also necessary to know the operating range of these parameters for laser surface hardening of steels for proper application in industry. The thermal analysis presented in this investigation addresses these issues.

It is generally preferable for laser heat treatment of steel to use a wider laser beam with a uniform heat intensity distribution for it enables uniform case depth [1]. This can be accomplished by using an expensive beam integrator or a beam manipulator system consisting of a segmented mirror system, or a two-axis vibratory system, or a system using toric mirrors. The second alternative, without adding significantly to either the complexity or the cost to the system, involves the use of a bimodal (TEM_{11}) shaped laser beam. The third alternative involves the use of a not-so-sharp focussed high-peak power, low order (TEM_{00}) mode Gaussian laser beam. In this investigation, a disk shaped heat source with a pseudo-Gaussian heat intensity distribution is used in the thermal analysis and the results compared with the experimental and semi-empirical analysis of Steen and Courtney [2].

2. Brief review of literature

Steen and Courtney [2] conducted a comprehensive investigation of laser transformation hardening of AISI 1036 (EN 8) steel using a 2 kW continuous wave CO_2 laser. They conducted a five level, full factorial design experiments by varying the power from 1.2 to 2.0 kW, the laser beam diameter from 1.6 to 5.8 mm, and the traverse speed from 25–400 mm/s and analyzed the results statistically. Based on the experimental fit of the data, they determined the depth of hardening as a function of the parameter $P/\sqrt{D_b v}$ and the onset of surface melting as a function of the parameter $P/D_b^2 v$. They prepared operating charts of the laser power versus the traverse velocity for various laser beam diameters, including operating lines for 0.1 mm hardening depth and surface melting lines for each beam diameter. In a subsequent publication (Davis et al. [3]), the authors pointed out that these relationships are strictly based on empirical relationships of the experimental data and have no physical or analytical basis. Nevertheless, their contribution is considered very significant in that they not only presented experimental results but also attempted to develop operating charts for the first time. There are, however, some limitations of this analysis as will be shown, based on the analytical results and a comparison with the exact relationships developed here.

Cline and Anthony [4] conducted one of the first comprehensive thermal analysis of the laser heat treatment with a scanning laser beam using a circular (or disc) shaped moving heat source with a Gaussian distribution of heat intensity under quasi-steady state conditions. They note the temperature distribution of the moving heat source to be asymmetric along the direction of the laser beam traverse. They also found that as the velocity of traverse increases, the maximum temperature decreases and shifts towards the trailing edge of the heat source, as Jaeger [5] and Carslaw and Jaeger [6] originally demonstrated, and the temperature decreases at various depths below the surface. The temperature under the laser beam was shown to decrease with increasing velocity for there is less time available for heating the material. They also showed that spot size has a strong influence on the maximum temperature attained as well as on the mechanism of deep penetration.

Lax [7] pioneered the modeling of the temperature distributions induced by laser irradiation in solids. He determined the spatial distribution of the temperature rise induced by a stationary Gaussian laser beam numerically for steady-state conditions by reducing it to a 1-D integral.

Sanders [8] developed a general solution for a moving circular disc heat source with a Gaussian distribution of heat intensity by applying the solutions of Lax [7] for a stationary point and a circular disc moving heat source. He then applied the general solution to determine approximate solutions for: (1) steady-state conditions (i.e., for slow scan speeds); (2) energy density solution (i.e., for fast moving beam heat sources where the

temperature rise is proportional to the integrated beam intensity); (3) surface absorption solution (i.e., for strongly absorbing material) for scanning beam problems. He also reported similar solutions for pulsed laser irradiation. He found the temperature rise to depend only on the ratio, υ $(= v\delta/4D)$ which is the ratio of scan speed (v) to the rate of heat diffusion ($4D/\delta$) in the solid and a geometric factor, γ $(= \alpha\delta/2)$ which is the ratio of the beam radius ($\delta/2$) to the absorption depth ($1/\alpha$). He also found the solution to approach the steady-state limit for small values of υ, the energy density limit for large values of υ, the surface absorption limit for large values of γ. While this relationship may be reasonable for approximate solutions, it will be shown in this paper that the temperature rise is a much more complex function of the laser beam diameter, beam velocity, and laser power. They enter in the integral limits of the special function as well as constants in the general solution (see Eq. (6)) as will be shown in this investigation.

Mazumdar and Steen [9] developed a 3-D heat transfer model for laser material processing with a circular (or disc) shaped moving heat source with a Gaussian distribution of heat intensity using a finite difference numerical technique. They limited their investigation to quasi-steady state conditions in that the thermal profile is considered steady relative to the position of the laser beam. The model was used to predict melting or fusion, HAZ, and thermal cycles in the neighborhood of laser-surface interaction.

Moody and Hendle [10] developed solutions for the temperature distribution for a moving CW laser beam with a Gaussian intensity distribution in a semi-infinite material. They introduced an interesting concept of using a highly elliptical beam at rapid scan rates to anneal large areas. It is an intriguing solution when limited by beam size, laser power intensity, and beam velocity. It can also be considered for expanding the region of laser annealing by taking advantage of the diffusing elliptic beam instead of a concentrated Gaussian beam.

Kou et al. [11] conducted an experimental and numerical analysis of laser transformation hardening of an AISI 1018 steel. They developed a 3-D heat flow model using the finite difference method. On the experimental side, they used a continuous wave CO_2 laser of 15 kW capacity along with a beam integrator that would provide a uniform distribution of heat intensity on a 12 mm $\times$ 12 mm square cross-section. Such a uniform laser beam of a square or a rectangular shape is ideal for surface transformation hardening due to uniform depth of the hardened case and the high coverage rate that can be obtained. They varied the beam power and the traverse speed and determined the onset of surface melting. The experimental results were compared with the results from the numerical analysis.

Chen and Lee [12] investigated transient temperature profiles in solids heated with a scanning laser with particular emphasis on the annealing of semiconductor materials. Their thermal analysis involved the use of a circular laser beam with a Gaussian distribution of heat intensity. They showed that the input energy density is constant when the input power is varied linearly with the scan velocity. They also contended the existence of a critical velocity (a/r_0) (which is defined as the ratio of the thermal diffusivity of the work material to the beam radius) below which the effects of the moving velocity becomes practically negligible. In the present investigation of laser surface hardening of AISI 1036 steel, the critical velocity for different beam radii used (using the conditions used by Steen and Courtney [2]) are in the range of 2.1–7.625 cm/s which is much lower than the values of the traverse velocities used in practice.

Ashby and Easterling [13] and Li et al. [14] investigated transformation hardening of hypo- and hypereutectoid steels, respectively, using a scanning laser beam. Two continuous wave CO_2 lasers (0.5 and 2.5 kW) were used in this study. The beam diameter was varied from 1–10 mm and the beam velocities in the range of 2–30 mm/s. The measured absorptivity was reported to be 0.7 ± 0.03 with an appropriate absorbent coating. They considered both Gaussian as well as "top hat" or uniform energy density distributions. As can be expected, the profile produced by the "top hat" was more uniform than that of the Gaussian beam. They developed approximate solutions for the heat flow and combined them with the kinetic models to predict the microstructure and hardness variations with depth from the surface due to laser transformation hardening. They developed diagrams which show the combination of process variables, such as energy density, beam radius, and depth below the surface for a given microstructure and the associated hardness profile.

Davis et al. [3] developed a thermal model for laser hardening of steel. They considered each of the conditions that is required for surface transformation hardening in their analysis, namely: (1) the material must reach the A_3 temperature of steel for austenitizing; (2) it must remain above this temperature for a sufficient time for carbon diffusion to take place (the time required for the carbon diffusion to take place is estimated as 0.003 s); and (3) it must then be quenched rapidly to transform austenite into martensite (the cooling rate of $\sim 10^3$°C/s).

Festa et al. [15] and Festa [16] developed simplified thermal models for laser and electron beam surface hardening. They developed a relationship between the hardening depth as a function of austenitization temperature and Peclet number for 1-D stationary and 2-D uniform strip moving heat source problems. They compared the analytical results with the experimental results in the literature and found a good correlation (maximum deviation being $\sim$9.1%).

Usually, the thermal properties of carbon steels are a strong function of temperature. In laser transformation

hardening, significant temperature gradients can be generated in the vicinity of the laser beam. The question is at which temperature, should the thermal conductivity be taken in the analysis, as only one value can be used in the analytical method. Isenberg and Malkin [17] and Kuo et al. [11] addressed this issue of variation of thermal conductivity with temperature. They found that the errors would be minimal so long as the thermal conductivity is taken close to the transformation temperature (or the melting temperature) as the case may be and not at room temperature. Komanduri and Hou [18] also conducted a similar analysis for the arc welding process and compared it with the FEM analysis of Tekriwal and Mazumdar [19]. The latter was conducted considering variable thermal properties. Komanduri and Hou [18] found the error to be <5–10% so long as the thermal conductivity is taken close to the transformation temperature. Significant errors were found using the room temperature thermal conductivity value. In this investigation, we have taken the thermal conductivity at the transformation temperature (A_{c3}) which is the same as that used by Steen and Courtney. This way, our analytical results can be compared with their semi-empirical analysis based on experimental results and the error can be minimized by not taking the thermo-physical properties at room temperature; instead at the transformation temperature (A_{c3}).

It can be seen from the above brief review of literature that most of the analyses to date were for quasi steady-state and very few, if any, for the transient conditions. Also, the boundary effects were not generally considered which assume significance when dealing with a narrow width work material. In this investigation, an attempt was made to develop general equations (both transient and quasi steady-state) taking into account the boundary effects. The analysis enables the determination of temperature at any point on the surface including close to the heat source but also the temperature profiles with variation in depth. It can also plot the variation of temperature from transient to steady-state conditions and determine the time required to reach steady-state conditions. Also, using this analysis, operational regions involving critical velocity for no surface melting on one end and critical velocity for a given hardening depth, say, 0.1 mm on the other, for different laser powers and beam diameters are developed.

3. Thermal model of the surface transformation hardening by a scanning laser beam

Fig. 2 is a schematic of the heat transfer model used for the example of surface transformation hardening of gears (see Fig. 1). When the moving laser beam (heat source) approaches either of the boundaries *a–a* or *b–b*, the boundary effects assume significance and cannot be

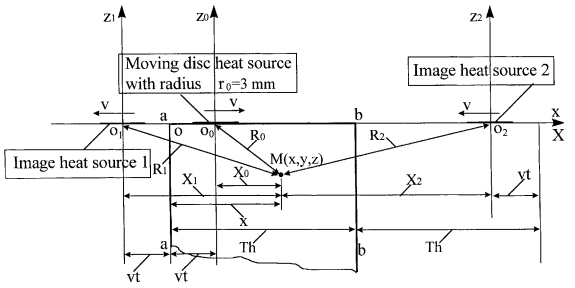

Fig. 2. Schematic of the heat transfer model for laser surface transformation hardening of gears.

neglected. Consequently, two image heat sources corresponding to the two boundaries o_1 and o_2 need to be considered. The width of the gear tooth is considered large compared to the thickness of the layer where the temperature rise during heat treatment is considered. These points in the layer are near the surface where the laser beam impinges but far from the opposite involute surface boundary of the gear tooth (see Fig. 1). Thus the boundary effect on the opposite involute surface can reasonably be ignored. Referring to Fig. 2, o_0, o_1, and o_2 are the centers of the primary and the two image heat sources, respectively. ox is the x-axis of the absolute coordinate system, o_0X, o_1X and o_2X, are the X-axes of the three moving coordinate systems related to the primary and the two image heat sources, respectively. The moving coordinate system moves along with the relevant heat sources at the same velocity and in the same direction.

The heat source is considered as a moving circular disc heat source (with a Gaussian heat intensity distribution) of radius r_0, cm, a heat liberation rate of q_{pl}, J/s, and moving with a traverse speed of v, cm/s. The moving disc heat source can be considered as a combination of a series of concentric segmental moving ring heat sources of radii r_i (r_i varying from 0 to r_0). The solution of a moving ring heat source for a semi-infinite conduction medium is given by [20]:

$$\theta_M = \frac{q_{\mathrm{rg}} v}{8\lambda a \pi^{3/2}} \mathrm{e}^{-XV} \int_{\omega=0}^{v^2 t/4a} \frac{\mathrm{d}\omega}{\omega^{3/2}} \exp\left(-\omega - \frac{u^2}{4\omega}\right) \times I_0\left[\frac{r_0 V^2}{2\omega}\sqrt{\left(X + \frac{2\omega}{V}\right)^2 + y^2}\right], \quad (1)$$

where $V = v/2a$, $u = V\sqrt{r_0^2 + X^2 + y^2 + z^2}$, $X, y, z,$ are the coordinates of point M in the moving coordinate system, and r_0 is the radius of the ring heat source. Eq. (1) is used as a basis for the derivations to follow.

The heat liberation rate q_{rg} of a segmental ring heat source is given by

$$q_{\mathrm{rg}} = q_0 2\pi r_i \,\mathrm{d}r_i, \quad (2)$$

where q_0 is the heat liberation intensity of a circular disc heat source, in J/cm^2 s. For a uniform distribution on a

circular disc heat source, it is a constant (given by $q_0 = q_{\rm pl}/(\pi r_0^2)$). For a Gaussian distribution, it is a function of r_i – the larger the r_i, the smaller the value of q_0. When $r_i = 0$, q_0 has its maximum value. When $r_i \to r_0, q_0 \to 0$. The approximate functional relationship for a pseudo-Gaussian distribution is given by

$$q_0 = C \exp\left[-\left(\frac{3r_i}{r_0}\right)^2 \right]. \tag{3}$$

The coefficient C is determined by integrating the heat liberation rates of all the segmental ring heat sources from $r_i = 0$ to $r_i = r_0$ and equating it to the total heat liberation rate of the disc heat source $q_{\rm pl}$, i.e.,

$$q_{\rm pl} = \int_{r_i=0}^{r_i=r_0} {\rm d}q = \int_{r_i=0}^{r_i=r_0} C \exp\left[-\left(\frac{3r_i}{r_0}\right)^2 \right] 2\pi r_i \,{\rm d}r_i. \tag{4}$$

Here,

$$2r_i\,{\rm d}r_i = {\rm d}(r_i^2) = r_0^2 \frac{{\rm d}(r_i^2)}{r_0^2} = r_0^2\,{\rm d}\left(\frac{r_i^2}{r_0^2}\right) = r_0^2\,{\rm d}z,$$

where $z = \left(\frac{r_i}{r_0}\right)^2$.

Substituting, z and $r_0^2\,{\rm d}z$ for $(r_i/r_0)^2$ and $2r_i\,{\rm d}r_i$ in Eq. (4), we get

$$q_{\rm pl} = \pi r_0^2 C \int_{z=0}^{z=1} {\rm e}^{-9z}\,{\rm d}z = \pi r_0^2 C \left| -\frac{{\rm e}^{-9z}}{9} \right|_{z=0}^{z=1} \approx \frac{\pi r_0^2 C}{9}$$

or $C = \dfrac{9q_{\rm pl}}{\pi r_0^2}$.

Substituting $(9q_{\rm pl})/(\pi r_0^2)$ for C in Eq. (3), we get

$$q_0 = \frac{9q_{\rm pl}}{\pi r_0^2} \exp\left[-\left(\frac{3r_i}{r_0}\right)^2 \right].$$

Substituting q_0 in Eq. (2), the heat liberation rate of each segmental ring heat source (from a disc heat source of Gaussian distribution) is given by

$$q_{\rm rg} = \frac{9q_{\rm pl}}{\pi r_0^2} \exp\left[-\left(\frac{3r_i}{r_0}\right)^2 \right] 2\pi r_i\,{\rm d}r_i = \frac{9q_{\rm pl}}{r_0^2} \exp\left[-\left(\frac{3r_i}{r_0}\right)^2 \right] 2r_i\,{\rm d}r_i.$$

Using Eq. (1), the differential temperature rise at any point $M(X,y,z)$ caused by this segmental ring heat source is given by (considering the origin of the moving coordinate system to coincide with the ring center)

$$ {\rm d}\theta_M = \frac{9q_{\rm pl}v}{4\lambda a\pi^{3/2}r_0^2} {\rm e}^{-(3r_i/r_0)^2} r_i\,{\rm d}r_i\, {\rm e}^{-XV} \int_{\omega=0}^{v^2t/4a} \frac{{\rm d}\omega}{\omega^{3/2}} \times \exp\left(-\omega - \frac{u^2}{4\omega} \right) I_0\left[\frac{r_i V^2}{2\omega} \sqrt{\left(X + \frac{2\omega}{V}\right)^2 + y^2} \right], \tag{5}$$

where $V = v/2a$, $u = V\sqrt{r_i^2 + X^2 + y^2 + z^2}$. The temperature rise at point $M(X,y,z)$ caused by the entire circular disc heat source with a Gaussian distribution of heat intensity is given by

$$\theta_M = \frac{9q_{\rm pl}v}{4\lambda a\pi^{3/2}r_0^2} {\rm e}^{-XV} \int_{r_i=0}^{r_i=r_0} {\rm e}^{-(3r_i/r_0)^2} r_i\,{\rm d}r_i \int_{\omega=0}^{v^2t/4a} \frac{{\rm d}\omega}{\omega^{3/2}} \times \exp\left(-\omega - \frac{u^2}{4\omega} \right) I_0\left[\frac{r_i V^2}{2\omega} \sqrt{\left(X + \frac{2\omega}{V}\right)^2 + y^2} \right]. \tag{6}$$

Referring to Fig. 2, the temperature rise at any point M and at any time t caused by each of the three heat sources (i.e., the primary moving disc heat source (θ_{M0}) and its two image heat sources (θ_{M1}) and (θ_{M2}), respectively) is given by

$$\theta_{M0} = \frac{9q_{\rm pl}v}{4\lambda a\pi^{3/2}r_0^2} {\rm e}^{-X_0V} \int_{r_i=0}^{r_i=r_0} {\rm e}^{-(3r_i/r_0)^2} r_i\,{\rm d}r_i \int_{\omega=0}^{v^2t/4a} \frac{{\rm d}\omega}{\omega^{3/2}} \times \exp\left(-\omega - \frac{u_0^2}{4\omega} \right) I_0\left[\frac{r_i V^2}{2\omega} \sqrt{\left(X_0 + \frac{2\omega}{V}\right)^2 + y^2} \right], \tag{7}$$

$$\theta_{M1} = \frac{9q_{\rm pl}v}{4\lambda a\pi^{3/2}r_0^2} {\rm e}^{-X_1V} \int_{r_i=0}^{r_i=r_0} {\rm e}^{-(3r_i/r_0)^2} r_i\,{\rm d}r_i \int_{\omega=0}^{v^2t/4a} \frac{{\rm d}\omega}{\omega^{3/2}} \times \exp\left(-\omega - \frac{u_1^2}{4\omega} \right) I_0\left[\frac{r_i V^2}{2\omega} \sqrt{\left(X_1 + \frac{2\omega}{V}\right)^2 + y^2} \right], \tag{8}$$

$$\theta_{M2} = \frac{9q_{\rm pl}v}{4\lambda a\pi^{3/2}r_0^2} {\rm e}^{-X_2V} \int_{r_i=0}^{r_i=r_0} {\rm e}^{-(3r_i/r_0)^2} r_i\,{\rm d}r_i \int_{\omega=0}^{v^2t/4a} \frac{{\rm d}\omega}{\omega^{3/2}} \times \exp\left(-\omega - \frac{u_2^2}{4\omega} \right) I_0\left[\frac{r_i V^2}{2\omega} \sqrt{\left(X_2 + \frac{2\omega}{V}\right)^2 + y^2} \right]. \tag{9}$$

Using the principle of superposition, the total temperature rise at any point M and at any time t is given by

$$\theta_M = \frac{9q_{\rm pl}v}{4\lambda a\pi^{3/2}r_0^2} \int_{r_i=0}^{r_i=r_0} {\rm e}^{-(3r_i/r_0)^2} r_i\,{\rm d}r_i \sum_{n=0}^{n=2} {\rm e}^{-X_nV} \int_{\omega=0}^{v^2t/4a} \frac{{\rm d}\omega}{\omega^{3/2}} \times \exp\left(-\omega - \frac{u_n^2}{4\omega} \right) I_0\left[\frac{r_i V^2}{2\omega} \sqrt{\left(X_n + \frac{2\omega}{V}\right)^2 + y^2} \right], \tag{10}$$

where

$$u_0 = R'_0 v/2a, \quad u_1 = R'_1 v/2a, \quad u_2 = R'_2 v/2a,$$
$$R'_0 = \sqrt{r_i^2 + X_0^2 + y^2 + z^2},$$
$$R'_1 = \sqrt{r_i^2 + X_1^2 + y^2 + z^2},$$
$$R'_2 = \sqrt{r_i^2 + X_2^2 + y^2 + z^2},$$
$$X_0 = x - vt, \quad X_1 = -(x + vt), \quad X_2 = 2\mathrm{Th} - x - vt.$$

Eqs. (6) and (10) are for transient conditions. For application to quasi-steady state conditions, theoretically the time t should be considered as ∞, i.e., the upper limit of the second integration in these equations, namely, $v^2 t/4a = \infty$. It has been shown [20] that when this upper limit $\to 5$, the temperatures calculated by these equations approach a constant value, i.e., when the upper limit is >5, no matter how large, the results of the calculations would have the same value indicating quasi-steady state conditions. It is, therefore, not necessary to consider $t = \infty$ in practice. Instead, a finite value, such as 5, in this case, can be used. Thus, Eqs. (6) and (10) can be used for quasi-steady state conditions by merely substituting 5 for the upper limit of the second integration $v^2 t/4a$. Using this relationship, the time required for reaching the quasi-steady state can be estimated, as

$$t_{\text{quasi-steady}} \approx 20a/v^2. \tag{11}$$

4. Results and discussion

4.1. Transient thermal analysis and boundary effects

In many practical applications, both transient and boundary effects can be significant and should not be neglected. A typical case is the laser surface hardening of gears (as shown in Figs. 1 and 2) which is analyzed in this investigation. Appropriate processing parameters including the laser power, the traverse velocity, and the beam diameter as well as the average thermal properties of the work material are given in Table 1 [2].

Fig. 3(a) shows the temperature rise distribution along the X-axis (refer to Fig. 2) at various instants of time (i.e., from $t = 0.016$ to 0.064 s) without the influence of the boundaries a–a and b–b. These plots were obtained using Eq. (6) (for $y = 0$ and $z = 0$) and the moving coordinate system. Point $X = 0$ is the location of the center of the circular disc heat source. It can be seen that longer the interaction time, the higher is the temperature rise. It can also be seen that the maximum temperature rise shifts towards the trailing edge of the heat source with time. The computational results also indicate (not shown in Fig. 3(a)) that when $t \geqslant 0.048$ s, the temperature rise distribution for various times are nearly the same which indicates that quasi-steady state has been reached. As derived earlier, the time for establishing the quasi-steady state can be calculated using Eq. (11), i.e.,

$$t_{\text{quasi-steady}} \approx 20a/v^2 \approx 20 \times 0.061/5^2 \approx 0.049 \text{ s}.$$

Figs. 3(b)–(d) are plots showing the effect of one boundary (on the left of the heat source or at the trailing edge) on the temperature rise distribution at different laser interaction times t (i.e., from $t = 0.016$ to 0.048 s). At $t = 0.016$ s, the center of the moving disc heat source has moved a distance $vt = 5 \times 0.16 = 0.8$ or 0.8 mm from the left edge. Thus, the distance between the heat source center and the left boundary a–a is 0.8 mm. At the same time, the corresponding image heat source has also moved a distance of 0.8 mm in the opposite direction. Therefore, the distance between the image heat source center and the left boundary a–a is 0.8 mm. Referring to Fig. 3(b) (with the point $X = 0$ denoted as the location of the center of the primary moving disc heat source) the left boundary a–a at $t = 0.016$ s is located at $X = -0.8$ mm and the center of the image heat source at $X = -1.6$ mm. Fig. 3(b) shows the two corresponding temperature rise distribution curves due to the primary and image heat sources. They are the same as the temperature rise distribution curve shown in Fig. 3(a) for $t = 0.016$ s but in the opposite direction to each other. The actual temperature rise distribution on the work surface at the right side of the boundary a–a is the result of the superposition of the two curves at the right side of the boundary. Fig. 3(b) shows the combined effect of the temperature rise distribution at $t = 0.016$ s. Figs. 3(c) and (d) show similar temperature rise distributions at $t = 0.032$ and 0.048 s, respectively, due to the effect of the boundary a–a. It can be seen that longer the time, the longer is the distance between the centers of the primary and the image heat sources and less is the influence of the boundary.

Fig. 4 shows the summary results of the calculations (using Eq. (10)) taking into account the influence of the boundaries, a–a and b–b. The temperature rise distribution curves obtained for $t = 0.016$, 0.032, and 0.048 s are identical to the combined temperature rise curves shown in Figs. 3(b)–(d) without showing per se the temperature rise distributions caused only by the image

Table 1
Laser processing parameters and the thermal properties of the work material [2]

Beam power, P	500 W
Absorptivity, C_{absorp}	0.8
Effective beam power, P_{eff}	400 W
Scanning velocity, v	5 cm/s
Beam spot radius, r_0	3 mm
Thickness of the gear, Th	25 mm
Thermal conductivity, λ_{Ac3}	0.339 J/s cm °C
Thermal diffusivity, a	0.061 cm^2/s

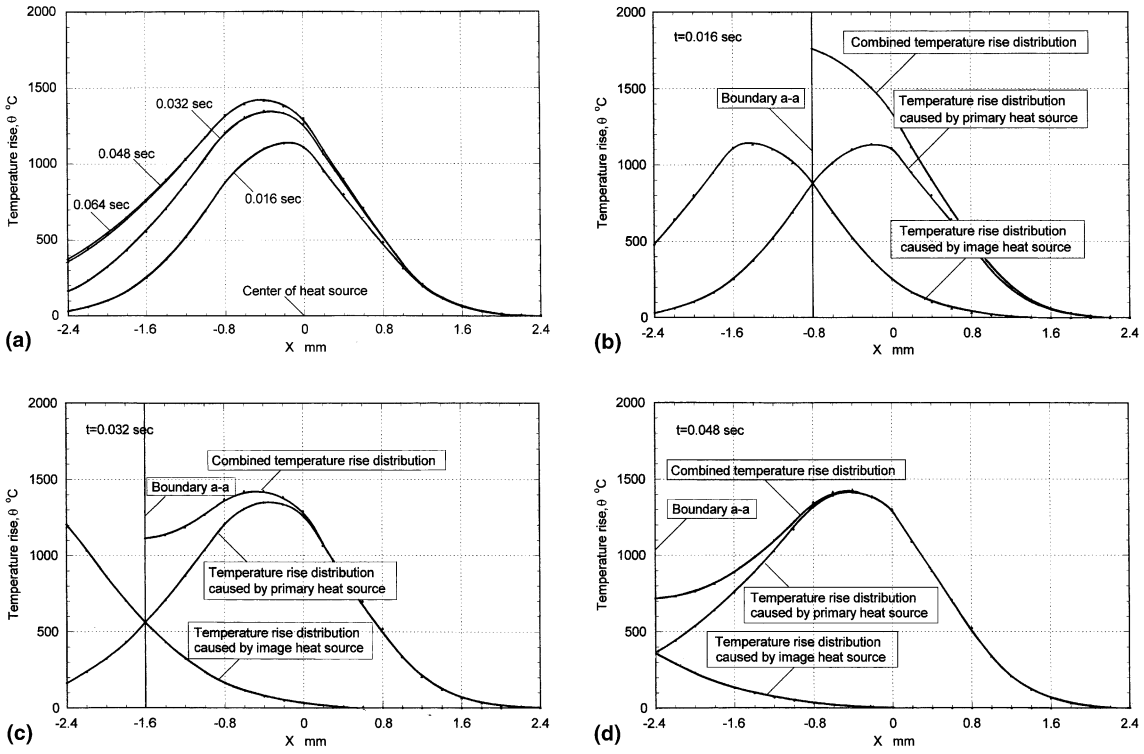

Fig. 3. (a)–(d) Temperature rise distribution along the X-axis (refer to Fig. 2) at various instants of time and combined temperature rise distribution due to primary and image heat sources.

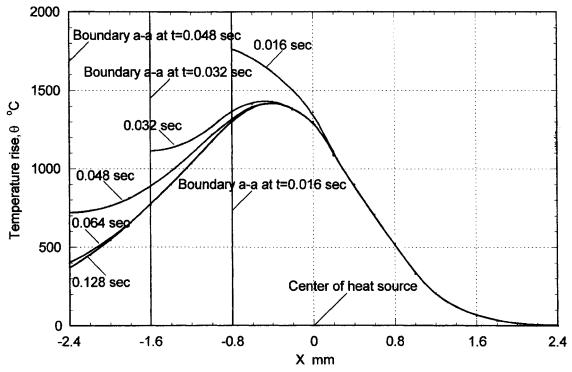

Fig. 4. Summary results of the temperature rise distributions due to primary and image heat sources (see Fig. 3).

heat source or the primary heat source. It may be noted that during this time, the right side boundary b–b (see Fig. 2) is relatively far from the primary heat source. So, its effect on the temperature rise around the area near by the primary heat source is not noticeable.

Figs. 5 and 6 are isotherms of various temperatures of interest on the top surface ($z = 0$, in plane x–o–y at different times (from $t = 0.016$ to 0.080 s) for Fig. 5 and (from $t = 0.468$ to 0.500 s) for Fig. 6 obtained using Eq. (10). Figs. 5(a)–(e) are the temperature contours obtained during the transient stage while Figs. 6(a)–(c) are the same isotherms obtained during quasi-steady state conditions. The effect of the boundary a–a, especially on the 775°C contour is noticeable in the early stages of Fig. 5 by way of stretching of this isotherm towards the boundary a–a. Similarly, the effect of the boundary b–b, especially on the 775°C contour is noticeable in the later stages of Fig. 6 again by way of stretching of this isotherm towards the boundary b–b. But this is hardly noticeable for the contours of the isotherms of 1370° (except at the very beginning (Fig. 5(a)) or at the very end (Fig. 6(c)) of the scanning process when the boundary effects are very high because this temperature is rather high and the percentage of the boundary effect in the total value is comparatively low. Fig. 6(a) shows a set of typical quasi-steady state (without noticeable boundary effects) isotherms of 775°C (phase transition temperature) and 1370°C (close to but lower than the melting point). The shape and size of the isotherms are found to be nearly constant from $t = 0.128$ to 0.468 s (the corresponding centers of the primary moving disc heat source are located in the range of $x = 6.4$ to 23.4 mm). In this range, no isotherm of melting temperature is detected, i.e., no surface melting. Figs. 6(b) and (c) show the same isotherms at the time

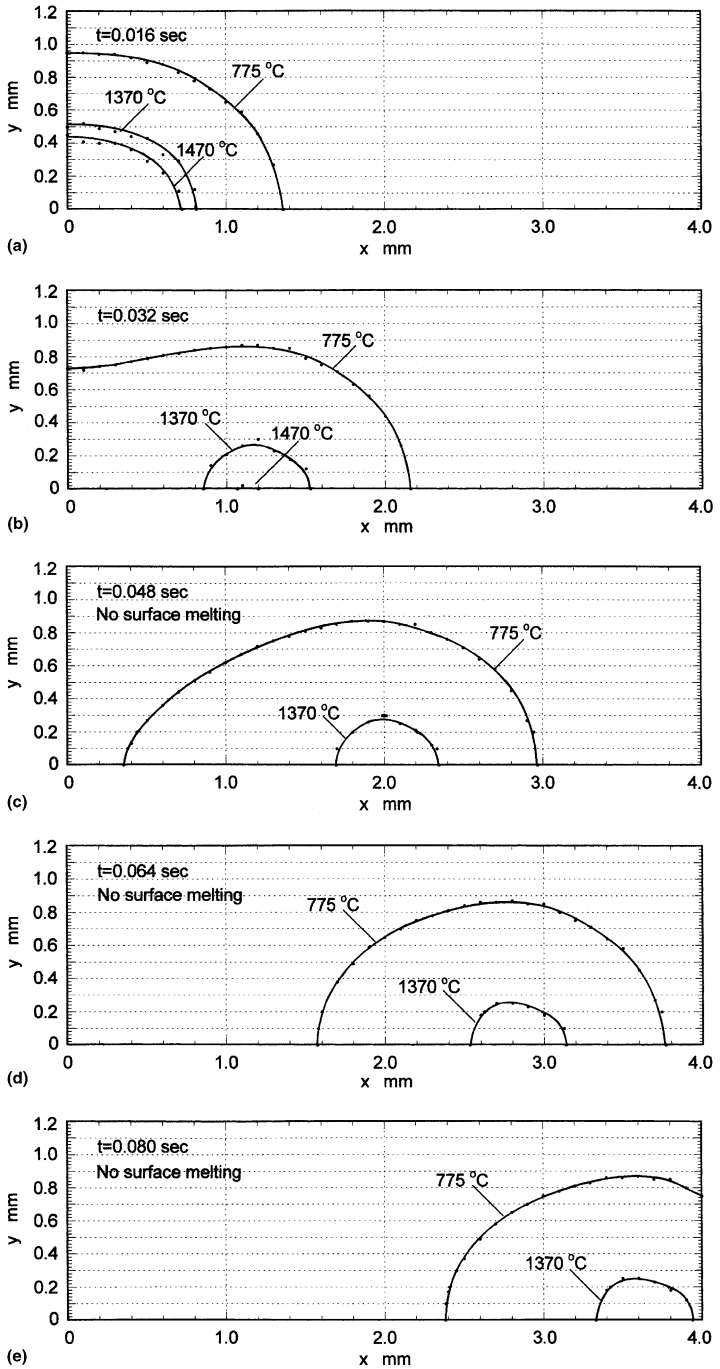

Fig. 5. (a)–(e) Isotherms of various temperatures of interest on the top surface ($z = 0$, in plane x–o–y) at different times (from $t = 0.016$ to 0.080 s).

when the centers of the heat source are very close to the right side boundary b–b. It can be seen that the boundary effect raises the right side of the contours of these isotherms quite significantly compared to the plots for the quasi-steady state (dotted lines). In Figs. 5(a) and 6(c), the appearance of the isotherms of the melting temperature (1470°C) show a strong influence of the boundaries a–a and b–b when the heat source is close to them.

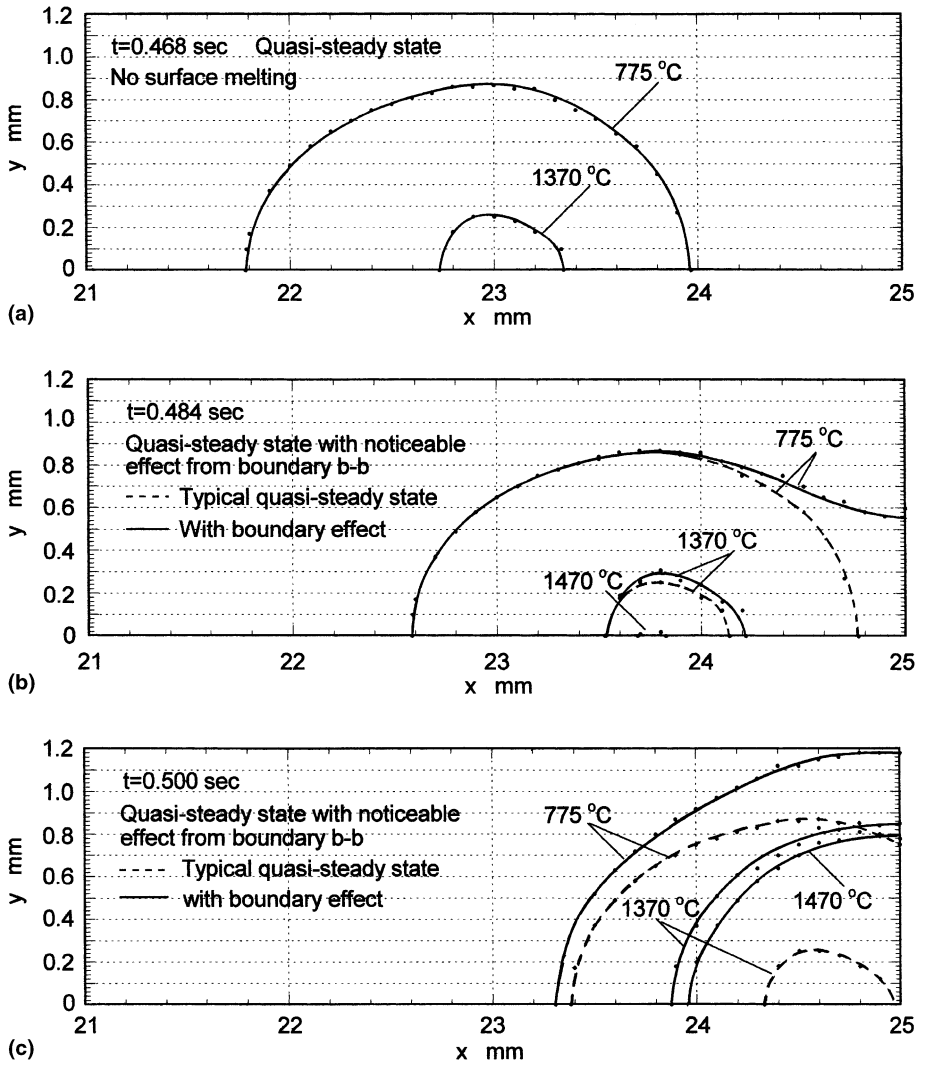

Fig. 6. (a)–(c) Isotherms of various temperatures of interest on the top surface ($z = 0$, in plane x–o–y) obtained during quasi-steady state conditions at different times (from $t = 0.468$ to 0.500 s).

Figs. 7(a) and (b) are the isotherms of 775°C in the x–o–z plane ($y = 0$) at various instants of time (from $t = 0.016$ to 0.080 s for Fig. 7(a) and from $t = 0.452$ to 0.500 s for Fig. 7(b)). It can be seen that from $\sim t = 0.048$ s, a stable depth of this isotherm (0.28 mm) has reached which remains unchanged until $\sim t = 0.484$ s. Correspondingly, in the range of $x = 2.4$ to 24.2 mm, the depth of hardening is ~0.28 mm. That means for ~87% of the scanning travel (from $x = 0$ to $x = 25$ mm), a constant thickness of hardened layer results. At the very beginning ($t = 0$ to 0.032 s, or $x = 0$ to 1.6 mm), the depth of hardening varies from 0 to 0.30 mm (due to transient conditions and the effect of boundary a–a). Similarly, towards the end ($t \rightarrow 0.50$ s or $x \rightarrow 25$ mm) the depth of hardening increases to 0.39 mm (again due to the effect of boundary b–b).

Figs. 8(a) and (b) are isotherms of 1370°C (lower but close to the melting temperature) and 1470°C (melting temperature) in the x–o–z plane ($y = 0$). It can be seen that at $t = 0.064$ s, a stable depth for the 1370°C isotherm has reached which remains unchanged until $\sim t = 0.468$ s. Correspondingly, in the range of $x = 3.2$ to $x = 23.4$ mm, the stable depth of this isotherm is ~0.031 mm. That means for ~78% of the scanning travel (from $x = 0$ cm to $x = 25$ mm) no surface melting is experienced. Only at the very beginning, i.e., when $t = 0.016$ s, surface melting appears (due to the influence of the boundary a–a). Its depth varies from 0 to 0.068 mm in the period of $t = 0$ to 0.016 s. After $t = 0.016$ s, the depth of the isotherm of the melting temperature diminishes rapidly due to decreasing influence of boundary a–a. Similarly, towards the end ($t \rightarrow 0.50$ s or $x \rightarrow 25$

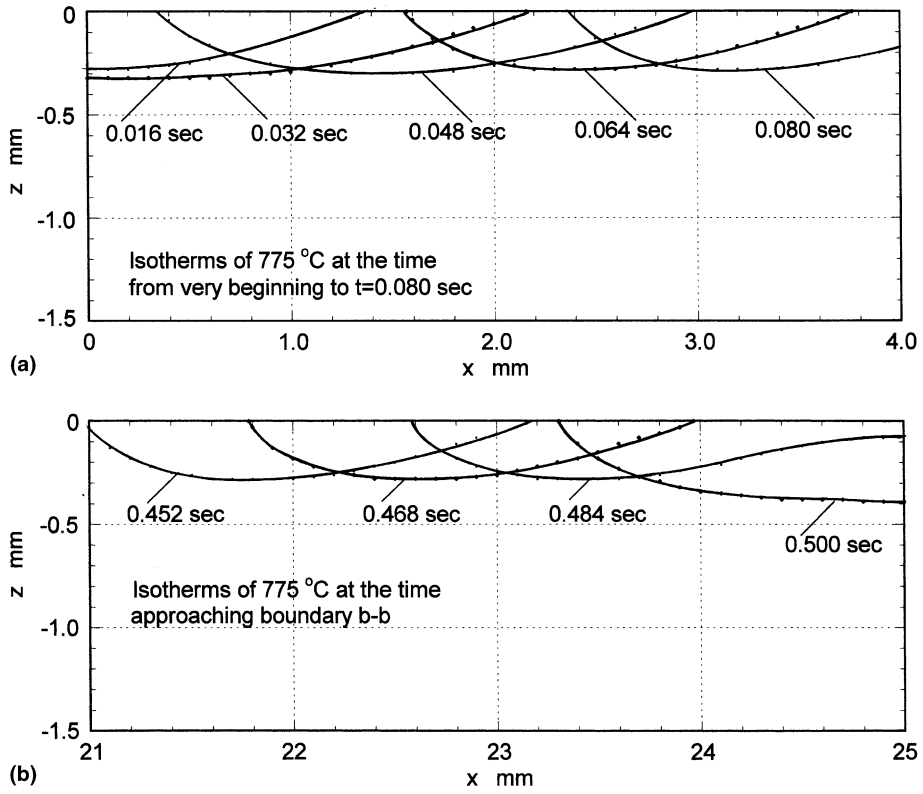

Fig. 7. Isotherms of 775°C in the x–o–z plane ($y = 0$) at various instants of time: (a) from $t = 0.016$ to 0.080 s; and (b) from $t = 0.452$ to 0.500 s.

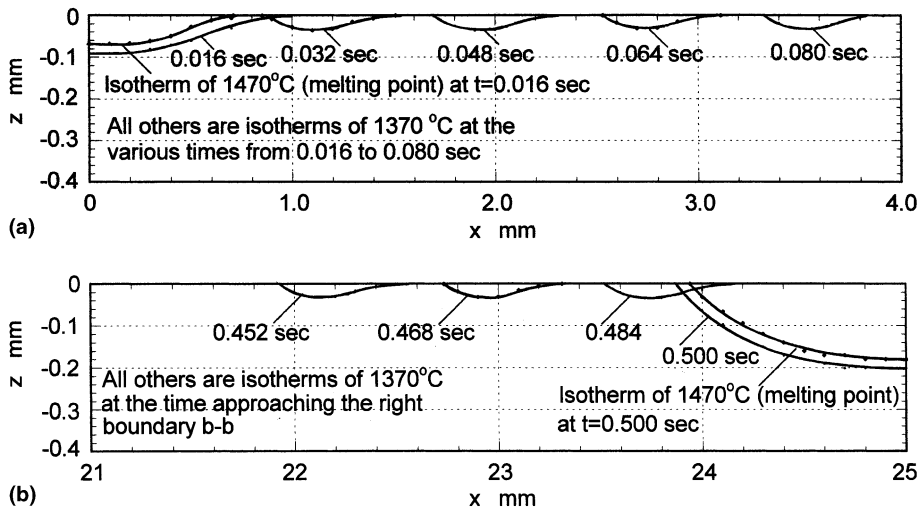

Fig. 8. (a) and (b) Isotherms of 1370°C (lower but close to the melting temperature) and 1470°C (melting temperature) in the x–o–z plane ($y = 0$).

mm) the surface melting appears again and reaches a maximum value of ~0.18 mm (due to the influence of boundary b–b). Also, note the depth of the melt zone is higher towards the end than at the beginning because one is already quasi-steady state while the other is at the very beginning of the transient state.

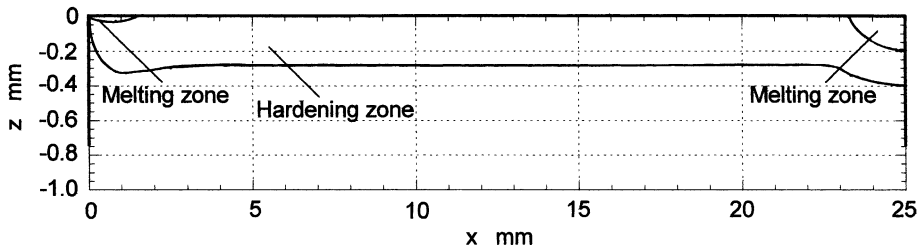

Fig. 9. Variation of the hardening zone under the surface after one traverse of the laser beam scanning. The thickness of the hardened layer is ≈0.28 mm for most of the length. Also, melting has occurred at entry and exit.

Fig. 9 shows the resulting hardening zone under the surface after one traverse of the laser beam scanning with the parameters used in Table 2 [2]. The thickness of the hardened layer is ~0.28 mm for most of the length. It also shows the areas (entry and exit) where melting has occurred. At the very beginning, the thickness of the melt zone is ~0.068 mm and towards the end it is ~0.18 mm. Fig. 10 is a schematic showing the area where the temperature is higher than the phase transition point at any given instant after the quasi-steady state has been established. This area is moving with the moving disc heat source at the same velocity v and will be self-quenched by conduction into the cold material beneath the surface. The depth of hardening is nearly the same as the depth of the zone where the temperature had been higher than the phase transition temperature.

Table 2
Laser processing parameters and metallurgical and thermal properties of the work materials used in the optimization studies [2]

Laser beam power, P	500, 750, 1000, 1250, 1500, 1750, 2000 W
Laser beam diameter, D_b	1.6, 2.6, 3.7, 4.8, 5.8 mm
Work material	AISI 1036 (EN 8) steel
Melting temperature	1470°C
Phase transition temperature	775°C
Thermal conductivity (mean), λ_{Ac3}	0.339 W/cm °C
Thermal diffusivity (mean), a	0.061 cm^2/s
Absorptivity	0.8

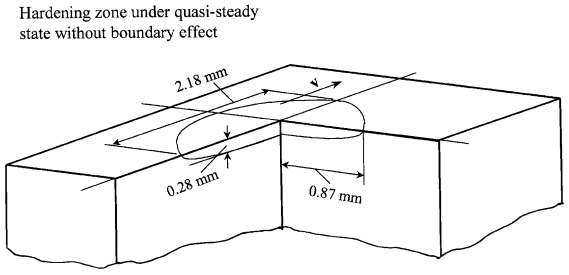

Fig. 10. Schematic showing the area where the temperature is higher than the phase transition point at any given instant after the quasi-steady state has been established.

Based on the above analysis, it can be seen that the parameters of the laser beam scanning for surface transformation hardening are not optimal even though most part of the process is satisfactory. The resulting surface temperatures are high near the two edges resulting in melting. It indicates that the selected power is somewhat high or the selected scanning velocity somewhat low at the very beginning and during the last moments of each scanning period. In fact, this effect is more pronounced towards the exit than at the entrance due to the reason mentioned above. For good laser surface hardening practice, i.e., without the melt pool, it is necessary to alter the process parameters towards the last stage of the process, if one were to use the same laser parameters given in Table 2 [2]. For this, it is necessary to adopt a different strategy involving reduced power or increased scanning velocity, or switch-off power altogether towards the end of the laser scanning cycle. This can be accomplished quite easily with most NC operated machine tools. Such a strategy was recently developed for welding of thin plates [21] and can be extended to the laser surface hardening process readily.

In the following, a procedure for the optimization of process parameters for laser surface hardening, namely, laser power, P, beam diameter, D_e, and scanning velocity, V within the two constraints, namely, critical velocity for no melting and critical velocity for a hardening depth of 0.1 mm for an AISI 1036 steel (EN 8) will be considered. This will enable the determination of the operating regime for laser surface hardening. It will be shown that this range is somewhat narrow due to the above constraints. The results of the analysis are compared with the experimental and semi-empirical analytical results of Steen and Courtney [2].

4.2. Optimization of process parameters

As mentioned in Section 2, Steen and Courtney [2] conducted a five level, factorial design of experiments for

surface hardening of an AISI 1036 (EN 8) steel using a continuous wave CO_2 laser at various conditions of laser power (1.2, 1.4, 1.6, 1.8, and 2.0 kW), beam diameter (1.6, 2.6, 3.7, 4.8, and 5.8 mm), and traverse velocity (25, 50, 100, 200, and 400 mm/s) (Table 2). It would have been beneficial had the experimental results been tabulated in their valuable paper. Since their work will be compared with the analytical results of the present investigation, it will be discussed in some detail here.

Steen and Courtney [2] conducted a statistical analysis of the experimental results. They initially fitted a response surface for depth of hardening using laser input parameters, namely, the laser power, P, scanning velocity, V, and the laser beam diameter, D_b. However, the expression generated was very complex and difficult to use or interpret the results. Hence, they attempted an alternate empirical approach.

Fig. 11 shows the variation of the parameter $P/\sqrt{D_b v}$ with the depth of hardening, z. It can be seen from the figure that the scatter of this parameter ($P/\sqrt{D_b v}$) with depth of hardening is quite significant with the scatter increasing with increasing hardening depth. Using a regression analysis of the experimental data (Fig. 11), Steen and Courtney arrived at the following relationship for the hardening depth z.

$$z = -0.10975 + 3.02P/\sqrt{D_b v}. \tag{12}$$

As an example, they considered the case of hardening depth z of ~0.1 mm, for if the wear is to exceed this value, the component in service would most likely loose its accuracy of size and geometrical shape and needs replacement. Fortuitously, the scatter is small or negligible in the range of hardening depth of up to 0.1 mm. Substitution of $z = 0.1$ mm in Eq. (12) yields

$$P/\sqrt{D_b v} = (0.1 + 0.10975)/3.02 = 0.06945$$

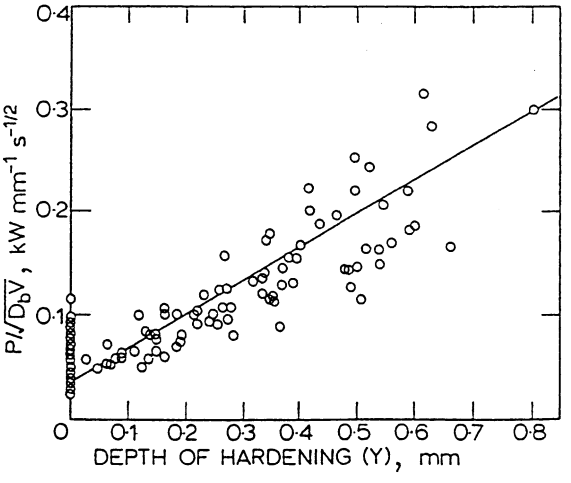

Fig. 11. Variation of the parameter $P/\sqrt{D_b v}$ with the depth of hardening, z after Steen and Courtney [2].

or

$$v = 207.305\frac{P^2}{D_b}. \tag{12'}$$

Eq. (12′) indicates that for a given depth of hardening, the parameter $P/\sqrt{D_b v}$ is a constant. For example, for the case of $z = 0.1$ mm, it is 0.06945. Using Eq. (12′), Steen and Courtney developed a series of plots of critical scanning velocity for 0.1 mm hardening depth versus power for different beam diameters, as shown by the dotted lines in Fig. 12(a). Only when the scanning velocity v is at or below the corresponding curve, the hardening depth can reach or exceed 0.1 mm, otherwise it will be <0.1 mm.

Figs. 12(a) and (b) show for various beam diameters, the variation of the critical scanning velocity with the laser power for a hardening depth of 0.1 mm and for the onset of surface melting, respectively. The solid lines are the analytical results obtained in this investigation and the dotted lines are the semi-empirical results of Steen and Courtney using Eqs. (12′) and (13′), which are derived from the linear regression analysis of the experimental results. The solid lines are obtained using Eq. (6) and the parameters from Table 2 for quasi-steady state conditions (i.e., by substituting 5 for the upper limit of the second integration ($v^2t/4a$) in Eq. (6)).

It can be seen from Fig. 12(a) that the analytical results are not in good agreement with the semi-empirical plots of Steen and Courtney. This is not because the analytical results do not agree with the experimental results but due to the way the semi-empirical plots were made using the experimental results. Steen and Courtney considered the scanning velocity to be proportional to the square of the laser power, P and inversely proportional to the diameter of the laser beam, D_b, for a hardening depth of 0.1 mm. The physical basis of this, however, is not clear. In fact, the authors themselves stated subsequently [3], that Eq. (12′) is strictly based on an empirical relationship of the experimental data and has no physical or analytical basis. Consequently, it is not too surprising that the semi-empirical results do not agree with the analytical results for laser surface hardening for a depth of hardening of 0.1 mm.

As stated in Section 1, for transformation hardening of steels, which is a diffusion process, a minimum interaction time of 10^{-2} s and a power density of 10^3–10^4 W/cm^2 are required for a hardening depth of 0.1 mm. The power density should not be too high for surface melting to take place and at the same time the duration should be long enough for a depth of hardening of 0.1 mm to take place.

Since the traverse velocity is assumed to vary with the square of the laser power, the traverse velocity according to the semi-empirical relationship, will increases rapidly as the laser power increases. As a result, there will be

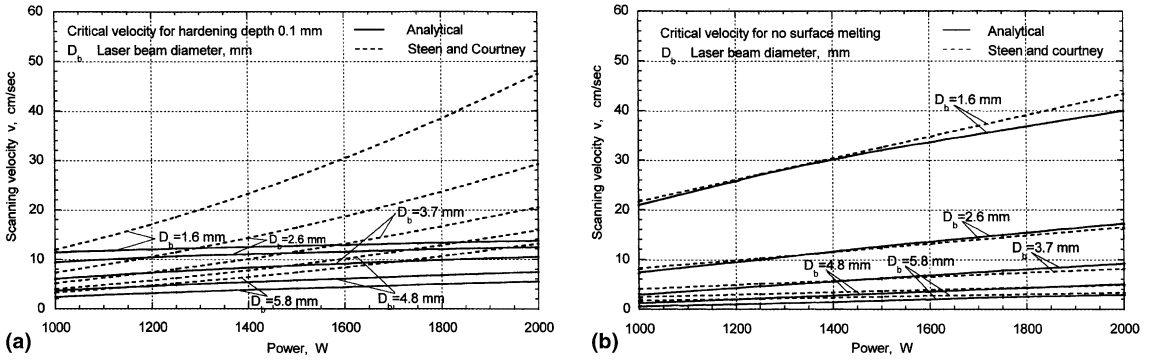

Fig. 12. (a) and (b) Variation of the critical scanning velocity for a hardening depth of 0.1 mm and for no surface melting, respectively, with the laser power for different beam diameters. The solid lines are analytical results of the current investigation and the dotted lines are the semi-empirical plots of Steen and Courtney [2].

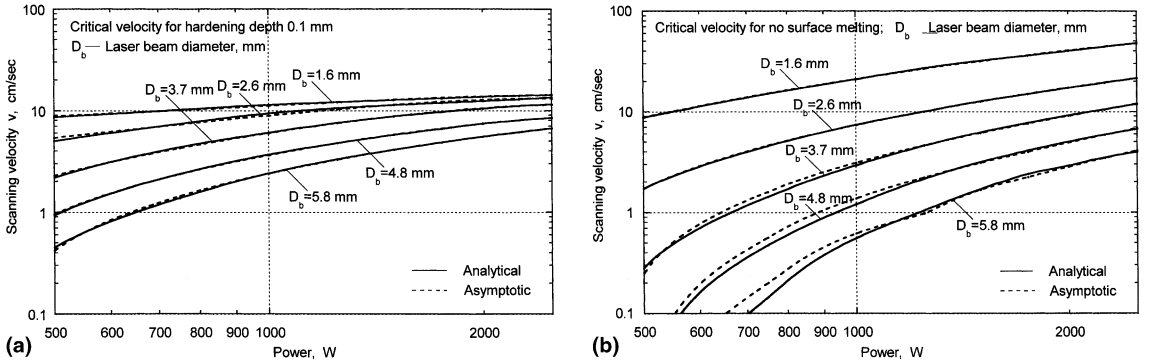

Fig. 13. (a) and (b) Variation of the critical scanning velocity for a hardening depth of 0.1 mm and for no surface melting, respectively with the laser power for different beam diameters. The solid lines are analytical results of the current investigation and the dotted lines are the best fit asymptotic curves using Eqs. (14) and (15), respectively.

insufficient time for laser transformation hardening to take place to a depth of 0.1 mm (see Fig. 12a).

Based on further analysis of the experimental data, it was found that when the laser power is higher than 1.2 kW, for all possible combinations of laser beam diameters and traverse velocities, using Eq. (12′), no surface hardening can take place at a depth of hardening of 0.1 mm, for there is insufficient time for transformation hardening to take place, which is a diffusion-controlled process. In other words, for these cases, the scanning velocities are over estimated using Eq. (12′), namely, $v = 207.305(P^2/D_b)$. In the optimization for laser hardening, one should consider two factors simultaneously, namely, sufficient time for 0.1 mm hardening depth and insufficient time for surface melting to take place. The analytical method presented here (Figs. 14(a)–(d)) takes into account both the factors for optimization of the process parameters for laser transformation hardening.

Steen and Courtney similarly considered the case of critical scanning velocity for no surface melting for an AISI 1036 (EN 8) steel. Based on linear regression of the experimental results, they found the surface temperature rise T to be proportional to $P/(D_b^2 v)$. Thus

$$P/(D_b^2 v) = C\lambda T. \tag{13}$$

For a given work material, the critical melting temperature T_{melt} and the thermal conductivity λ were assumed to be constants (for e.g., for an AISI 1036 (EN 8) steel, $T_{melt} = 1470°C$, $\lambda_{A_3} = 0.339$ J/s cm °C). For the onset of surface melting, the term $P/(D_b^2 v)$ is a constant $\sim 2000 \pm 1000$ J/cm^3. Based on the experimental results, Steen and Courtney assumed this constant to be 1800 J/cm^3. Thus, for the onset of surface melting, the critical velocity is given by

$$v = \frac{P}{1800 D_b^2}. \tag{13′}$$

Based on Eq. (13′) for an AISI 1036 (EN 8 steel), Steen and Courtney made a series of linear plots of critical scanning velocity for the onset of surface melting for various laser powers and beam diameters as shown by

the dotted lines in Fig. 12(b). No surface melting takes place when the selected scanning velocity v is above the corresponding curve but not at or below it, surface melting occurs. Good agreement can be seen between the analytical results and the semi-empirical plots of Steen and Courtney, except at large laser powers (>1.5 kW) and at the smallest laser beam size (1.6 mm diameter). Eq. (13′) appears reasonable as the scanning velocity is considered to be proportional to the power intensity. As stated in Section 1, for surface melting, the power density levels should be on the order of 10^5–10^7 W/cm^2. For example, the power density for the case, where $P = 2000$ W, $D_b = 1.6$ mm, is about 1×10^5 W/cm^2. It is close to the lower limit for surface melting. If the scanning velocity is too high for the case of small beam diameter, the flash duration at the melting temperature on the surface may be too short and insufficient for surface melting. This was found to be the case for this example. Hence, the scanning velocity is estimated to be too high for the high power case when Eq. (13′) is used. Consequently, the velocity should be lower than Steen and Courtney's semi-empirical relationships and closer to the analytical results.

Based on the above discussion, it appears that the functional relationships Eqs. (12′) and (13′) developed on the basis of the regression analysis are very approximate at best especially for the transformation hardening to a depth of 0.1 mm. The actual relationship between various parameters, as will be shown in the following, are more complex (given by Eq. (6)) and need to be considered in detail for a comprehensive understanding of the thermal process of surface transformation hardening of steel by a traverse laser beam.

To determine the underlying reasons for the differences between these two sets of analytical data (for a hardening depth of 0.1 mm and for the onset of surface melting) with the respective semi-empirical plots of Steen and Courtney, it would be convenient to convert the exact functional relationships between the various parameters of laser transformation hardening with a scanning laser (as given in Eq. (6)) into a simpler mathematical expression, such as an asymptotic function that is sufficiently close to the original function. This is because the analytical solution is rather complex and several processing parameters are involved in the special functions as well as in some integration limits. Consequently, it is somewhat difficult to analyze this equation directly in terms of the processing parameters, namely, laser power and beam diameter. It is also clear from this equation that the relationship between the scanning velocity and the laser beam diameter and power is much more complex than that proposed by

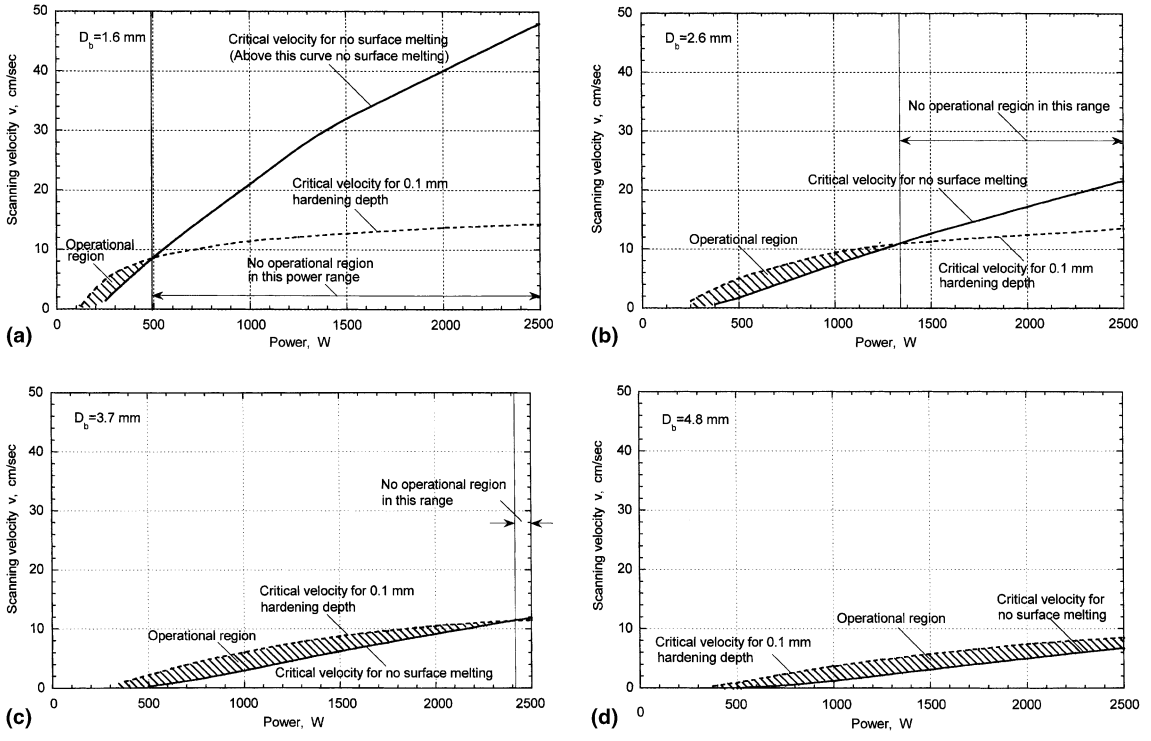

Fig. 14. (a)–(d) Optimization curves of the operating regions (by hatched lines) showing the variation of the scanning velocity with the laser power for various beam diameters, namely, 1.6, 2.6, 3.7, and 4.8 mm, respectively.

Steen and Courtney. The closest asymptotic curves to the solid lines (which are the results of calculations using the exact analysis of Eq. (6)) (in Fig. 12) are obtained by considering a polynomial expression.

Thus, the traverse velocity for the case of hardening depth of 0.1 mm is given by

$$v = A_1 + B_1 P + C_1 P^2, \tag{14}$$

where

$$A_1 = 17.279 - 87.148 D_b + 94.249 D_b^2, \tag{14a}$$

$$B_1 = -0.0015333 + 0.083841 D_b - 0.12433 D_b^2, \tag{14b}$$

$$C_1 = (0.31794 - 21.319 D_b + 33.964 D_b^2) \times 10^{-6}. \tag{14c}$$

Similarly, the traverse velocity for the case of no surface melting is given by

$$v = A + BP + CP^2, \tag{15}$$

where

$$A = -7.0201 + 10.808 D_b, \tag{15a}$$

$$B = 0.11567\, e^{-7.3709 D_b}, \tag{15b}$$

$$C = (-18.659 + 118.29 D_b - 246.32 D_b^2 + 171.18 D_b^3) \times 10^{-6}. \tag{15c}$$

It can be seen that the traverse velocities for a hardening depth of 0.1 mm and for no surface melting are expressed as functions of laser beam power and beam diameter (not merely as a linear function but a linear and a quadratic terms). Also, note that A, B, and C as well as A_1, B_1, C_1 (in Eqs. (14) and (15)) are not constants but functions of the beam diameter. This way the functional relationships can take into account the effect of process parameters more realistically, as will be shown in the following.

Figs. 13(a) and (b) show the variation of the critical scanning velocity for a hardening depth of 0.1 mm and for no surface melting, respectively, with the laser power for different beam diameters using the process parameters given in Table 2. The solid lines are obtained using the exact analysis (Eq. (6)) and the dotted lines using the asymptotic equations (Eqs. (14) and (15)). A good fit can be seen between them. A comparison of Eq. (13′) [$v = P/1800 D_b^2$] with Eq. (15) clearly shows that the former is somewhat over simplified. It shows that the critical velocity for the onset of surface melting is directly proportional to the laser power P and inversely to the square of the laser beam diameter D_b. It, also, implies that no matter how small the value of P is and/or how large the beam diameter D_b is, the velocity for the onset of surface melting can be obtained from Eq. (13′). This leads to an erroneous conclusion, namely, no matter how low the power density is, if the scanning velocity is low enough, surface melting will occur. Actually, when the power density is very low (when the laser beam power is very low or the beam diameter very large) surface melting will never takes place even when the scanning velocity is very low, even close to zero. Eq. (15), on the other hand, can be used satisfactorily to explain this phenomena. Referring to this equation, it can be seen that when D_b is large, the coefficient B will be very small, and the second term of Eq. (15) would not be able to compensate for the negative value of the first term to yield a positive value of velocity. As for the third term, it is also small when the power is low. For example, consider the case of a laser beam of diameter, $D_b = 0.58$ cm. Using Eqs. (15a)–(15c), $A = -0.7515$, $B = 0.001609$, and $C = 0.45292 \times 10^{-6}$, if $P_{eff} = 400$ W (that means the power density is very low, about 1.5×10^3 W/cm^3, it is nearly the lowest limit possible for laser heat treatment), the critical velocity for the onset of the surface melting is given by (using Eq. (15))

$$\begin{aligned} v &= -0.7515 + 0.001609P + 0.45292 \times 10^{-6} P^2 \\ &= -0.7515 + 0.6436 + 0.07247 \\ &= -0.0354 \text{ cm/s}. \end{aligned} \tag{16}$$

This means no surface melting will take place at the low power densities since the scanning velocity is negative (<0). Practically, the lowest scanning velocity is zero. Thus, at low power densities, even when the scanning velocity is reduced to zero, no melting on the surface takes place. But Eq. (13′) indicates that no matter how low the power density, surface melting will occur when the velocity is sufficiently low. This difference stems from the different considerations used for the relationships between the various parameters used in Eqs. (13′) and (15). In Eq. (13′) a simple proportional relationship was considered while in the analytical solution (Eq. (6)) the actual physical phenomena concerning the mechanism of temperature rise was considered as a starting point for its derivation.

Comparing Eq. (12′) ($v = 207.305(P^2/D_b)$) with Eq. (14), it can be seen that Eq. (12′) is somewhat simplified and the effect of power is exaggerated. Eq. (14), an asymptotic close to the analytical solution in the range of conditions used, shows that v is a complex function of P and P^2. The corresponding terms of P and P^2 have coefficients of a small number. Thus the effect of P^2 on the critical velocity for 0.1 mm hardening depth is rather weak than that shown by Eq. (12′). Consequently the solid lines calculated using the analytical solution (Eq. (6) or (14)) are flatter than the dotted lines (calculated using Eq. (12′)) as shown in Fig. 12(a).

In the following, the operating regions for different laser processing conditions for laser surface transformation hardening will be presented based on optimization of process parameters for no surface melting and

0.1 mm hardening depth. Figs. 14(a)–(d) show the variation of the scanning velocity with the laser power for various beam diameters, namely, 1.6, 2.6, 3.7, and 4.8 mm, respectively. In these figures, the critical velocity v for the onset of surface melting is shown by the solid lines and for the 0.1 mm hardening depth by the dotted lines. Here, a linear scale is used to show the natural relationships between relevant parameters. The scanning velocity should be higher than the solid line curve to avoid surface melting and lower than the dotted line for a hardening depth of not less than 0.1 mm.

It can be seen from Fig. 14(a) that for a laser beam diameter, $D_b = 1.6$ mm, in the power range 500–2500 W there is no operational region because in this range with such a small beam diameter, the mean power density is very high ($\sim 2.5 \times 10^4$ to 1.2×10^5 W/cm^2) and melting is imminent. However, at the lower power values, a small operating region is available but at very low scanning velocities which can be uneconomical in practice. It can also be seen from Figs. 14(a)–(d), the larger the laser beam diameter D_b is, the wider is the operational region. For $D_b = 2.6$ mm, the operational range of power is 250 to 1270 W and powers >1270 W can not be used. At this upper limit, the mean power density is $\sim 2.4 \times 10^4$ W/cm^2. For $D_b = 3.7$ mm, the operational range of power is 350 to 2310 W and powers >2310 W cannot be used. At this upper limit, the mean power density is $\sim 2.15 \times 10^4$ W/cm^2. It shows that for heat treatment there is an upper limit of mean power density. In this case, it is ~ 2.15–2.5×10^4 W/cm^2 which is in very good agreement with the recommended values (on the order of 10^4 W/cm^2) as indicated earlier. Overall, it can be seen that within the power considered, the scanning velocity range is rather limited (~2–10 cm/s) and the power range decreases with decreasing beam diameter. Also, the operating region can be seen to be somewhat limited. It may be noted that these plots are for quasi-steady state conditions and without the consideration of boundary effects. Using these plots, a set of operational parameters for 0.1 mm hardening depth without surface melting can be selected.

5. Conclusions

1. A general solution (transient as well as quasi-steady state) for the laser scan surface transformation hardening process using a disk heat source with pseudo-Gaussian heat intensity distribution was developed. It gives an exact relationship between the process parameters, such as the laser power, P, beam diameter, D_e, and traverse velocity, v of the beam relative to the workpiece and the various temperatures of interest. It can be used to calculate the temperature rise at any point and at any time on the surface or with respect to the depth around the moving disc heat source.
2. The technique was applied for laser surface transformation hardening of AISI 1036 (EN 8) steel gears taking into account the boundary effects which can be very significant at the beginning and the end of the laser hardening cycle. The analytical results were compared with the experimental results and the semi-empirical approach of Steen and Courtney [2]. The limitations of such an empirical approach were pointed out and more realistic plots of the variation of critical laser scanning velocity for no surface melting and a hardening depth of 0.1 mm with laser power for different laser beam diameters were presented.
3. Operating regions for different processing conditions for laser surface transformation hardening were presented based on the optimization of process parameters for no surface melting and 0.1 mm hardening depth. For small beam diameters, the mean power density can be very high ($\sim 2.5 \times 10^4$–1.2×10^5 W/cm^2) resulting in surface melting. The operating range was found to enlarge with increase in laser beam diameter. Overall, it can be seen that within the useful power range considered, the scanning velocity range is somewhat limited (~2–10 cm/s) and the power range decreases with decreasing beam diameter. It was also found that the operating regions are somewhat limited. Using these plots, a set of operational parameters for 0.1 mm hardening depth without surface melting can be selected.
4. The analytical solution for the temperature rise distribution (Eq. (6)), being exact, is somewhat complex with several process parameters involved in the special functions as well as in some integration limits. Consequently, it is difficult to analyze this equation directly in terms of the processing parameters, namely, laser power, P, traverse velocity, v and the beam diameter, D_b. However, by converting the exact functional relationships into simpler mathematical expressions, it is possible to investigate the effect of critical scanning velocity with the laser beam power, P and beam diameter, D_b more realistically. Such a function of critical scanning velocity was found to be of the form $v = A + BP + CP^2$, where A, B, C are not constants but functions of the laser beam diameter.
5. The analytical solutions give more accurate predictions that are closer to practice. They also provide a better insight into the physical process of laser transformation hardening of steels.

Acknowledgements

This project was initiated by a grant from the NSF US–China co-operative research project on the Thermal Aspects of Manufacturing. One of the authors (R.K) thanks Dr. Alice Hogen of NSF for facilitating this

activity and for her interest in this project. The authors are indebted to NSF for their continuing support to one of the authors (R.K) at OSU on the various aspects of the manufacturing processes. Thanks are due, in particular, to Drs. L. Martin-Vega, Kesh Narayan, K. Rajurkar, Delci Durham of the Division of Design, Manufacturing, and Industrial Innovation; to Dr. B.M. Kramer, of the Engineering Centers Division; and to Dr. Jorn Larsen Basse of the Tribology and Surface Engineering program. One of the authors (R.K) also thanks the MOST Chair for Intelligent Manufacturing for enabling in the preparation of the manuscript.

References

[1] J. Mazumder, Laser heat treatment: the state of the art, J. Metals (1983) 18–26.
[2] W.M. Steen, C.H.G. Courtney, Surface heat treatment of EN 8 steel using a 2 kW continuous-wave CO_2 laser, Metals Technol. (1979) 456–462.
[3] M. Davis, P. Kapadia, J. Dowden, W.M. Steen, C.H.G. Courtney, Heat hardening of metal surfaces with a scanning laser beam, J. Phys. D 19 (1986) 1981–1997.
[4] H.E. Cline, T.R. Anthony, Heat treating and melting material with a scanning laser or electron beam, J. Appl. Phys. 48 (9) (1977) 3895–3900.
[5] J.C. Jaeger, Moving sources of heat and the temperature at sliding contacts, Proc. Roy. Soc. NSW 76 (1942) 203–224.
[6] H.S. Carlsaw, J.C. Jaeger, Conduction of Heat in Solids, Oxford University Press, Oxford, UK, 1959.
[7] M. Lax, Temperature rise induced by a laser beam, J. Appl. Phys. 48 (9) (1977) 3919–3924.
[8] D.J. Sanders, Temperature distributions produced by scanning Gaussian laser beams, Appl. Opt. 23 (1) (1984) 30–35.
[9] J. Mazumder, W.M. Steen, Heat transfer model for CW laser material processing, J. Appl. Phys. 51 (2) (1980) 941–947.
[10] J.E. Moody, R.H. Hendel, Temperature profiles induced by a scanning CW laser beam, J. Appl. Phys. 53 (6) (1982) 4364–4371.
[11] S. Kou, D.K. Sun, Y.P. Lee, A fundamental study of laser transformation hardening, Metall. Trans. A 14 (1983) 643–653.
[12] I. Chen, S. Lee, Transient temperature profiles in solids heated with a scanning laser, J. Appl. Phys. 54 (2) (1983) 1062–1066.
[13] M.F. Ashby, K.E. Easterling, The transformation hardening of steel surfaces by laser beams – I. Hypo-eutectoid steels, Acta. Metall. A 32 (11) (1984) 1935–1948.
[14] W.-B. Li, K.E. Easterling, M.F. Ashby, Laser transformation hardening of steel-II hypereutectoid steels, Acta. Metall. 34 (8) (1986) 1533–1543.
[15] R. Festa, O. Manca, C. Naso, Simplified thermal models in laser and electron beam surface hardening, Int. J. Heat Mass Transfer 33 (11) (1990) 2511–2518.
[16] R. Festa, A comparison between models of thermal fields in laser and electron beam surface processing, Int. J. Heat Mass Transfer 31 (1) (1988) 99–106.
[17] J. Isenberg, S. Malkin, Effect of variable thermal properties on moving band source temperatures, ASME Paper No. 74-WA/Prod-5, 1974.
[18] R. Komanduri, Z.B. Hou, Thermal analysis of the arc welding process. Part II – effect of variation of thermophysical properties with temperature, Metall. Mater. Trans. B 2000 (in press).
[19] P. Tekriwal, J. Mazumdar, Finite element analysis of three dimensional transient heat transfer in GMA welding, Welding Res. Suppl. (1988) 150s–156s.
[20] Z.B. Hou, R. Komanduri, Magnetic field assisted finishing of ceramics – Part I: thermal model, Trans. ASME J. Tribol. 120 (1998) 645–651.
[21] R. Komanduri, Z.B. Hou, Thermal analysis of the arc welding process. Part I – general solutions, Metall. Mater. Trans. 31B (6) (2000) 1353–1370.